



Photoacoustic microscopy in tissue engineering

Xin Cai¹, Yu Shrike Zhang², Younan Xia^{2,*} and Lihong V. Wang^{1,*}

¹Department of Biomedical Engineering, Washington University, St. Louis, MO 63130, USA

²The Wallace H. Coulter Department of Biomedical Engineering, Georgia Institute of Technology and Emory University, Atlanta, GA 30332, USA

Photoacoustic tomography (PAT) is an attractive modality for noninvasive, volumetric imaging of scattering media such as biological tissues. By choosing the ultrasonic detection frequency, PAT enables scalable spatial resolution with an imaging depth of up to ~7 cm while maintaining a high depth-to-resolution ratio of ~200 and consistent optical absorption contrasts. Photoacoustic microscopy (PAM), the microscopic embodiment of PAT, aims to image at millimeter depth and micrometer-scale resolution. PAM is well-suited for characterizing three-dimensional scaffold-based samples, including scaffolds themselves, cells, and blood vessels, both qualitatively and quantitatively. Here we review our previous work on applications of PAM in tissue engineering and then discuss its future developments.

Introduction

Tissue engineering is an interdisciplinary, rapidly developing field that deals with the development of new tissue/organ substitutes to promote the healing or replacement of injured tissues [1–3]. In most cases, three-dimensional (3D) scaffolds are required to play a vital role in providing physical support and a controllable micro-environment for desired cell activity and tissue growth [4–7]. To optimize its performance in the regeneration of a specific tissue, the scaffold must possess appropriate properties, such as biocompatibility, biodegradability, tissue-matching mechanical strength, as well as proper porosity, pore size, and interconnectivity [8,9]. To this end, it is of great importance to examine, monitor, and quantitatively assess cell attachment, migration, proliferation, differentiation, and tissue formation within the scaffolds. In addition, there is also a strong need to monitor the alterations to the scaffolds themselves, such as changes in porosity, pore size, and degradation [10,11].

Despite many years of research, it remains a challenge to visualize the inside of scaffolds at high spatial resolution, deep penetration, and strong contrast in a non-invasive manner. The most widely used imaging modalities to characterize scaffold/tissue constructs include X-ray micro-computed tomography (micro-CT), scanning electron microscopy (SEM), laser-scanning optical

microscopy (LSM), optical coherence tomography (OCT), and magnetic resonance imaging (MRI). Micro-CT can penetrate the entire thickness of a scaffold/tissue construct up to several centimeters. However, the capability of micro-CT is limited by poor contrast for soft tissues and fluid-perfused scaffolds [12], unless a toxic contrast agent (*e.g.* osmium tetroxide) is administered [13–15]. SEM can provide fine resolution up to a few nanometers, but the penetration depth is essentially limited to the surface. In addition, it is invasive and requires dehydration and fixation of the biological samples such as cells and the extracellular matrix (ECM) [16]. Additionally, both micro-CT and SEM are based on ionizing irradiation that poses hazards to organisms. LSM, including confocal and multi-photon microscopy, has long been used for visualizing cells and angiogenesis in scaffolds [17,18]. However, because of strong light scattering, especially in the presence of blood, LSM has a limited tissue penetration of several hundred micrometers, and it also requires a fluorescent chromophore as the probe [19]. OCT has been demonstrated for label-free imaging of tissue/scaffold constructs at a relatively high resolution (~0.9 μm) [20], but it is rather difficult to distinguish the tissue and the scaffold in a sample because of their similar refractive indices. MRI has been employed to identify the deposition of ECM secreted by cells in scaffolds *in vivo* [21], and can be potentially used to evaluate cell differentiation [22]. Nevertheless, MRI suffers from relatively low spatial resolution (70–100 μm) and long image acquisition time. Therefore, new imaging techniques with high

*Corresponding authors: Xia, Y. (younan.xia@bme.gatech.edu), Wang, L.V. (lhwang@wustl.edu)

decade, the applications of PAT have been explored in both animals [29–32] and humans [33–36]. PAT systems have three major types: photoacoustic microscopy (PAM) [37], photoacoustic computed tomography (PACT) [38], and photoacoustic endoscopy (PAE) [39]. Among them, PAM uses direct point by point detection and raster scanning to generate an image.

In this review, we focus on PAM of 3D scaffolds or scaffold/tissue constructs for tissue engineering and regenerative medicine. We first introduce the fundamentals of PAM. Next, we highlight our previous work, which was essentially the first ensemble of applications of PAM in tissue engineering, including characterization of the properties of a porous scaffold, resolution of the spatial distribution of cells in a scaffold, and monitoring of the invasion of neovasculature into scaffolds, together with quantitative analyses in all cases. Finally, we point out some remaining issues and envision a few possible future developments.

Fundamentals of photoacoustic microscopy

In PAM, both the optical excitation and the ultrasonic detection are focused. The foci are configured coaxially and confocally. The laser fluence on tissue surface could be maintained well below or close to the American National Standards Institute (ANSI) safety limit [40].

For each laser shot, time-resolved ultrasonic detection produces a one-dimensional (1D), depth-resolved image (A-line) without mechanical scanning. Thus, a 1D line scanning produces a two-dimensional (2D) frame (B-scan) and a 2D raster scanning along the transverse plane produces complete volumetric (3D) information. Volumetric images can be viewed through either maximum amplitude projection (MAP) or direct 3D rendering. MAP is typically performed by projecting the maximum signal amplitude from each A-line onto the transverse plane, although projections along other axes are possible as well. Usually, PAM aims to image millimeters deep at micrometer-scale resolution. The axial resolution and the maximum penetration depth are inversely proportional to the central frequency of the ultrasonic transducer [41]. The axial resolution is on the scale of $\sim 10 \mu\text{m}$ [42,43], which is sufficient for most tissue engineering applications at the cellular level. It becomes inadequate only when subcellular resolution is required for applications in cell biology. The lateral resolution is predominantly determined by the tighter focus of the dual foci. This, in turn, can be used to further classify PAM into optical-resolution PAM (OR-PAM) [44,45] and acoustic-resolution PAM (AR-PAM) [37].

In OR-PAM (Fig. 1), a bright-field optical illumination, with a much tighter focus than the acoustic focus, is adopted to achieve

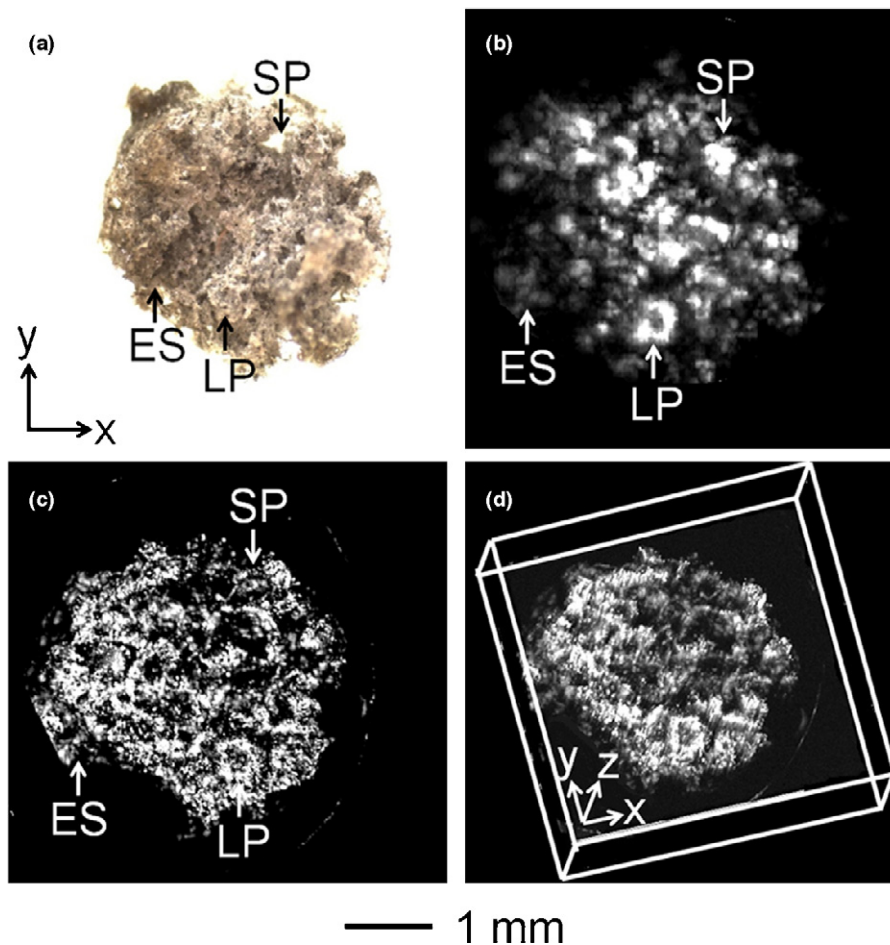


FIGURE 3

(a) An optical microscopy image of a porous PLGA scaffold incorporated with SWNTs. (b) An MAP image of the scaffold acquired by AR-PAM. (c) An MAP image of the scaffold acquired by OR-PAM. Note that matching features can be identified in these images (indicated by labeled arrows: LP, a large pore; SP, a small pore; ES, the edge of scaffold). (d) A 3D reconstruction image of the OR-PAM data.

Reprinted with permission from Ref. [12]. Copyright 2011 Mary Ann Liebert, Inc.

optical resolution [44]. The excitation light is collimated by a microscope objective to achieve optical focusing. A right-angle prism and a rhomboid prism sandwich a thin layer of silicone oil for acoustic-optical coaxial and confocal alignment. The interface between the prism glass and silicone oil provides optical transmission but acoustic reflection because of the matched optical refractive indices but mismatched acoustic impedances. A correction lens attached to the top surface of the right-angle prism is used to compensate for the optical aberration. OR-PAM provides lateral resolution ranging from a few hundred nanometers to a few micrometers, sufficient to resolve single cells or even subcellular structures [46–48]. However, the tissue penetration of OR-PAM is restricted to less than 1.2 mm because of the high optical scattering [44]. Although the imaging depth of OR-PAM is limited to the ballistic photon regime as that of pure optical microscopy, OR-PAM provides primarily optical absorption contrasts instead of conventional optical scattering or fluorescence contrasts.

In AR-PAM (Fig. 2), the optical focus is much wider than the ultrasonic focus and it is implemented through a dark-field

illumination. The light is reshaped by a conical lens to form a ring pattern [37,49]. The ring-shaped light is then weakly focused into the sample by an optical condenser. The generated photoacoustic waves are detected by a focused ultrasound transducer, which is located in the center of the optical condenser. Using an ultrasound transducer with a central frequency of 50 MHz, AR-PAM achieves a lateral resolution of 45 μm , an axial resolution of 15 μm , and a penetration depth of more than 3 mm [37]. In this depth range, the resolution is determined by ultrasonic detection because ultrasound scattering is much weaker than optical scattering in biological tissues and polymer scaffolds [50].

Photoacoustic microscopy characterization of porous scaffolds

It is important to characterize the properties of porous scaffolds – a critical component in tissue engineering – such as the porosity, pore size, and material degradation, in an effort to optimize their use in different applications. While conventional, destructive methods (*e.g.* SEM) are still widely used, a few techniques based

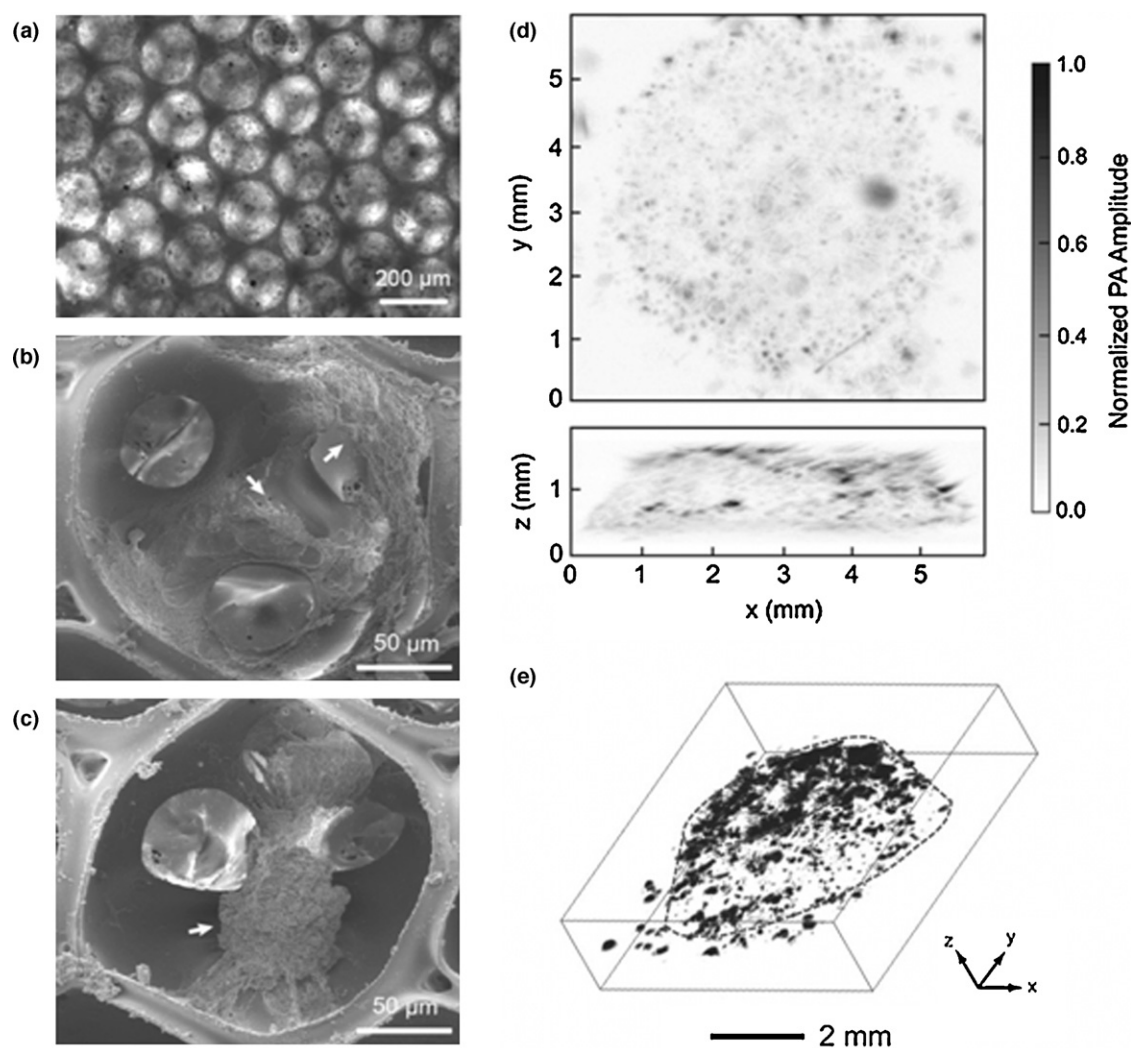


FIGURE 4

(a) A transmission optical microscopy image showing the melanoma cells grown in a PLGA inverse opal scaffold for 14 days. (b and c) SEM images showing individual melanoma cells or a cluster of melanoma cells grown in individual pores of a scaffold. (d) PAM coronal (top) and sagittal (side) MAP images. The black dots or patches correspond to melanoma cells. (e) A 3D reconstruction image, where the contour of the scaffold is marked by dotted lines.

Reprinted with permission from Ref. [65]. Copyright 2010 Elsevier.

on noninvasive imaging have been developed [20,51–54], which, however, largely suffer from the aforementioned limitations. Therefore, PAM has come into attention in fulfilling this job. In a recent demonstration, both OR-PAM [44] and AR-PAM [37] were employed to image and characterize poly(D,L-lactide-co-glycolide) (PLGA) scaffolds incorporated with single-walled carbon nanotubes (SWNTs) [55].

Fig. 3a shows an optical micrograph of the scaffold. A small quantity of SWNTs was introduced into the PLGA matrix to enhance the photoacoustic contrast from the scaffold [56,57], because PLGA itself could not generate sufficient photoacoustic signals to achieve sufficient contrast at the experimental wavelengths. Fig. 3b and c shows MAP images of the scaffold obtained by AR-PAM and OR-PAM, respectively, at an excitation wavelength of 570 nm. Fig. 3d shows a 3D depiction of the scaffold acquired by OR-PAM. The images of the scaffold obtained from PAM show clear details of the structure, which agree well with those obtained from optical microscopy. The common features that can be identified from the images are indicated by arrows (LP, a large pore; SP, a small pore; ES, the edge of scaffold). For this type of scaffold, AR-PAM and OR-PAM provided penetration depths of 1.7 mm and 660 μm , respectively. Thus, using PAM, a 3D scaffold can be conveniently and nondestructively examined to measure physical properties such as pore size and porosity.

The capability of PAM to resolve scaffolds under physiological conditions was demonstrated by imaging the SWNT-incorporated-scaffold either immersed in bovine blood or embedded in chicken tissue. According to the optical absorption spectra of SWNTs and blood [58,59], two wavelengths (570 nm and 638 nm) were chosen to spectrally differentiate the photoacoustic signals generated from blood and from the SWNT-incorporated scaffold. Under these simulated physiological conditions, OR-PAM was defocused to image a small portion of the scaffold at superficial depth, whereas AR-PAM was still able to penetrate the tissue/blood-covered scaffold to a depth of 1.7 mm.

PAM was further used to quantify the porosity and pore size of the SWNT-incorporated-scaffolds. For OR-PAM, the porosity and pore size of the scaffolds were estimated to be $86.5\% \pm 1.2\%$ and $153 \pm 15 \mu\text{m}$ (average diameter \pm standard error, $n = 4$), respectively. And for AR-PAM, the porosity and pore size were $81.8\% \pm 4.4\%$ and $167 \pm 24 \mu\text{m}$, respectively. These results agreed well with each other and with those measured by micro-CT ($88.6\% \pm 0.8\%$ and $145 \pm 9 \mu\text{m}$).

Photoacoustic microscopy imaging of living cells in porous scaffolds

Melanoma cells in scaffolds

Because melanoma cells contain naturally dark pigments, they exhibit strong intrinsic contrast for label-free PAM with high

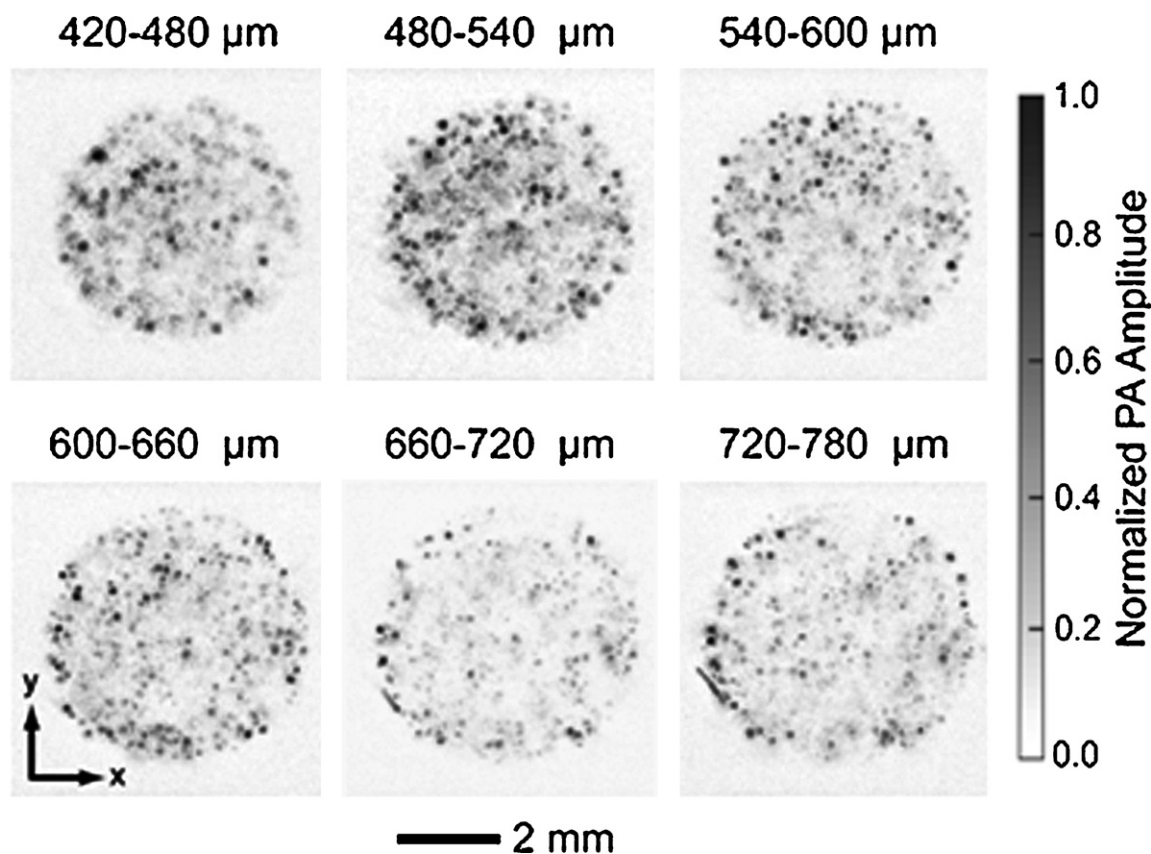


FIGURE 5

MAP PAM images of melanoma cells in a scaffold cultured for 14 days. The images were taken from different layers parallel to the top surface without slicing the scaffold. The first layer started at 420 μm beneath the surface, and the layer spacing was 60 μm .

Reprinted with permission from Ref. [65]. Copyright 2010 Elsevier.

sensitivity both *in vitro* [60,61] and *in vivo* [37,62]. The AR-PAM system was employed to image melanoma cells seeded in PLGA inverse opal scaffolds [63,64] for tissue engineering applications [65]. The inverse opal scaffolds represent a unique type of 3D porous scaffolds that have uniform pore sizes and a long-range ordered pore structure. These features can provide good interconnectivity throughout the entire scaffold to facilitate cell migration and nutrient/waste transport [9,66–68].

Fig. 4a–c shows the morphology of melanoma cells in PLGA inverse opal scaffolds. Under an optical microscope the cells were optically opaque (Fig. 4a), thus providing strong photoacoustic contrasts. From SEM images, melanoma cells, as marked by the arrows, have a typical size of 20–100 μm when they are fully stretched (Fig. 4b) or form cell clusters (Fig. 4c). The coronal (top view) and sagittal (side view) MAP images from PAM in Fig. 4d clearly show the spatial distribution of cells in the scaffold, penetrating the entire cell/scaffold construct with a thickness of around 1.5 mm. Fig. 4e shows a 3D depiction of melanoma cells in the scaffold. Individual cells or cell clusters could be identified (black dots or patches) in both 2D and 3D images. This penetration depth is much deeper than what LSM can achieve (~ 0.3 mm) when imaging scaffolds similarly seeded with melanoma cells [65].

Serial sections were further mapped with a layer thickness of 60 μm in the examined volume non-invasively without the need of physically slicing the scaffold (420–780 μm in depth, Fig. 5). The images clearly showed that PAM can resolve the spatial distribution of cells in the bulk of a thick scaffold. In another demonstration, both the dynamic and stationary methods were used for seeding and culturing cells in scaffolds, which were then evaluated using PAM. For the dynamic method, the cells were uniformly distributed throughout the 3D scaffold over the entire 14 days. For the stationary method, the cells were mainly distributed at the perimeter of the scaffold at 1 day post-seeding, whereas the distribution became uniform after 14 days because of cell migration, indicating that PAM can readily distinguish different patterns of cell distribution as well as cell migration.

In addition to qualitative imaging, it is even more challenging to temporally monitor and quantify cell proliferation in a 3D scaffold with relatively high spatial resolution. Fluorescence microscopy may be useful for long-term monitor if the cells are labeled with live-cell dyes [69], or with intrinsic fluorescent proteins [70]. However, photobleaching of the fluorescent dyes and proteins can be a problem, and cell mitosis can dilute the dyes as well. Shallow penetration depth comprises another limitation. By contrast, PAM is well-suited for chronologically monitoring and quantifying cell proliferation in individual scaffolds by taking advantages of strong contrast and deep penetration. Melanoma cells were seeded into PLGA inverse opal scaffolds and non-invasively imaged by AR-PAM at days 1, 3, 7 and 14 post-seeding. Time-course coronal MAP PAM images clearly show the proliferation of melanoma cells inside the same scaffold (Fig. 6a). Photoacoustic volumetric data were further utilized to quantify the cell numbers. The signal amplitude from the photoacoustic volumetric data was found to be linearly correlated with the number of cells in the scaffold [65]. From the calibration curve, the average cell numbers at days 1, 3, 7 and 14 were calculated to be 4.9×10^4 , 2.8×10^5 , 3.4×10^5 and 2.7×10^5 per scaffold, respectively. Fig. 6b plots the cell numbers calculated by PAM as a function

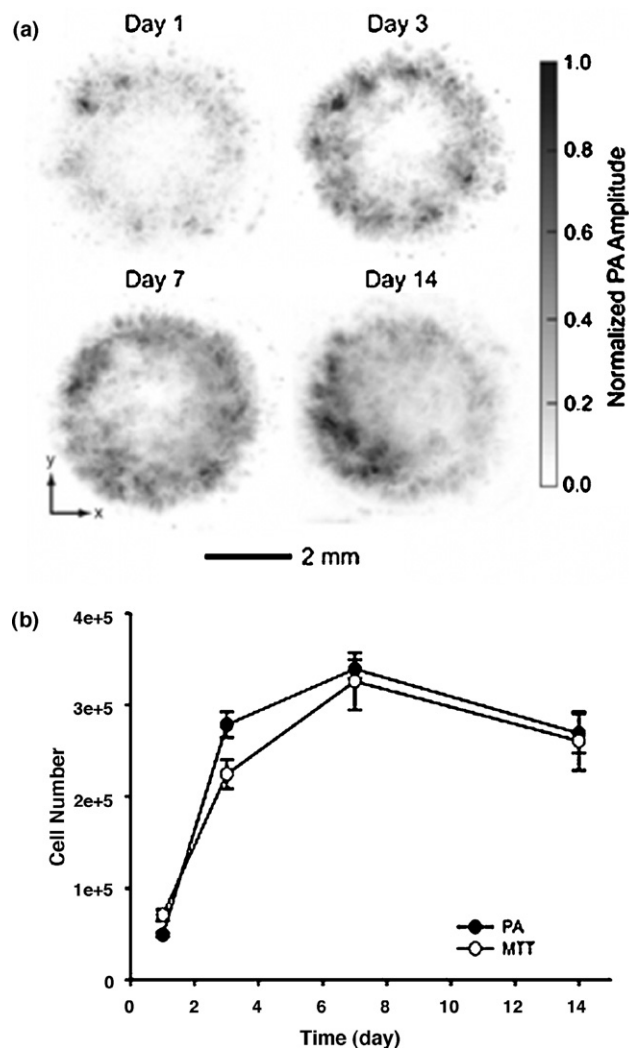


FIGURE 6

(a) Time course PAM images (coronal MAP of the entire volume) of melanoma cells in a typical PLGA inverse opal scaffold at 1, 3, 7 and 14 days post-seeding. (b) Quantitative analysis of melanoma cells in scaffolds derived from both the PAM volumetric data ($n = 4$) and the MTT assay ($n = 3$). The data are presented as mean \pm standard error. Reprinted with permission from Ref. [65]. Copyright 2010 Elsevier.

of time. The profile agreed well with the result from a parallel analysis where cell proliferation was measured using the conventional invasive 3-(4,5-dimethylthiazol-2-yl)-2,5-diphenyltetrazolium bromide (MTT) assay.

MTT formazan stained cells in scaffolds

All cells can potentially be imaged directly by PAM at some wavelengths because of their different intrinsic absorption contrasts with the background from absorption of such as melanin, cytoplasm and nuclei. However, extrinsic contrast agents are widely used to enhance image contrasts and achieve deeper penetration depth. Several types of contrast agent, such as reporter gene expression [71–74] and gold nanoparticles [75,26,76–79], have been demonstrated for use with PAM imaging of cells. Another simple method has recently been devised based on MTT formazan for stable and non-toxic staining of various types of cells, allowing PAM imaging in both 2D and 3D [80]. MTT is a water-soluble

tetrazole that can be metabolized and reduced to insoluble MTT formazan in living cells [81,82]. The MTT assay has been widely used to evaluate cell viability, metabolic activity, and proliferation. The suspension of MTT formazan crystals in phosphate buffered saline shows strong absorption in the spectral region of 500–700 nm, with a peak at ~650 nm. As a result, the MTT formazan crystals formed inside living cells can be directly used to remarkably enhance their contrast for PAM. This contrast mechanism is general and applicable to essentially all types of metabolically active cells such as fibroblasts, stem cells, and tumor cells.

In a demonstration, we seeded fibroblasts in a PLGA inverse opal scaffold and then stained the cells with MTT formazan. The coronal and sagittal MAP PAM images could be used to resolve the spatial distribution of fibroblasts in the scaffold with a penetration

depth over 1.5 mm (Fig. 7a, dark dots). The 3D distribution of cells could be rendered from the volumetric PAM data (Fig. 7b). It was further proven that MTT could also stain cells in a dense matrix rather than the highly porous scaffolds. In this case, fibroblasts were cultured in a PLGA inverse opal scaffold filled with cross-linked alginate hydrogel. Again, the images (Fig. 7c) clearly showed identifiable cells throughout the scaffold after incubating with MTT solution. The features on the surface of the scaffold were matched with those shown in the optical micrograph (Fig. 7d), indicating good accuracy of PAM. Chronological PAM was further employed to quantify the proliferation of cells. At 6 h, 3 days and 7 days post-seeding of fibroblasts, the scaffolds were incubated with MTT and then imaged with AR-PAM (MAP images shown in Fig. 7e). The integration of photoacoustic signal amplitudes

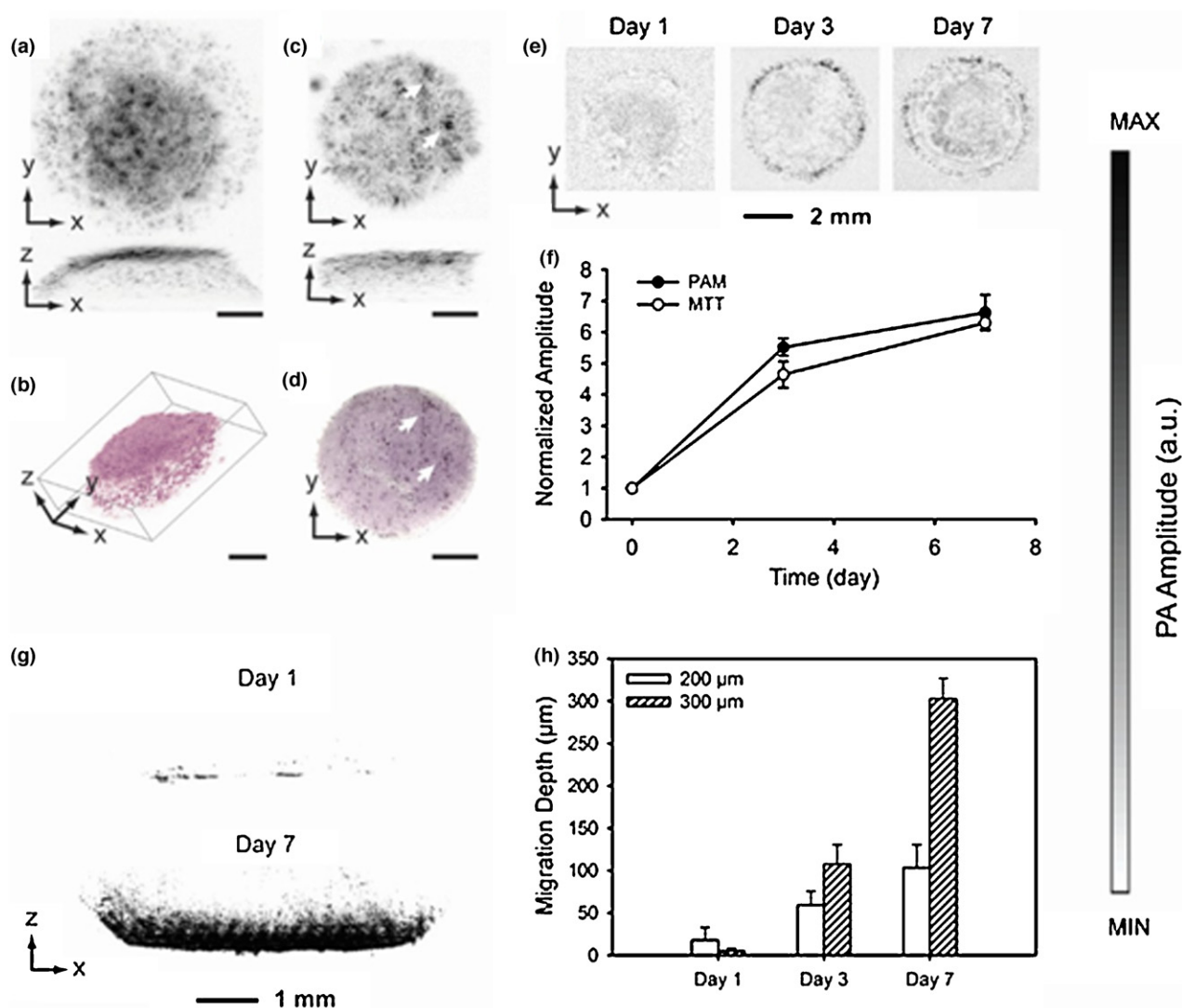


FIGURE 7

(a) MAP PAM image of fibroblasts cultured in an inverse opal scaffold, followed by MTT staining for 3 h; (b) 3D rendering of the volumetric PAM data in (a); (c) MAP PAM image of fibroblasts cultured in an inverse opal scaffold filled with cross-linked alginate hydrogel, followed by incubation with MTT for 4 h; and (d) an optical micrograph showing the same scaffold as in (c). As indicated by arrows, the features in PAM and optical microscopy well matched each other. Scale bars in (a–d): 1 mm. (e) PAM chronological images of fibroblasts grown in inverse opal scaffolds (MAPs in the 600–660 µm layers from the top surface) at 6 h, 3 days and 7 days; and (f) quantification of cell numbers in the scaffolds as determined by volumetric PAM data and parallel MTT biochemical assays. (g) PAM images showing cell invasion profile at days 1 and 7 into inverse opal scaffolds with a pore size of 300 µm; and (h) quantification of average cell penetration depths in scaffolds with pore sizes of 200 and 300 µm, respectively, as determined by PAM virtual biopsy. Reprinted with permission from Ref. [80]. Copyright 2011 Wiley-VCH.

corresponded to the total number of cells. The results measured at days 3 and 7 were normalized to what was obtained at 6 h. In Fig. 7f, the curve clearly shows how the cells proliferated over time. The proliferation profile derived from PAM matched what was obtained from the traditional destructive MTT cell viability assay based on the spectrophotometry method. The scope of the application was further expanded to a cell invasion assay, in which fibroblasts were induced to invade into PLGA inverse opal scaffolds with two different pore sizes of 200 and 300 μm . As shown by the sagittal MAP PAM images (Fig. 7g), by day 7, the cells had invaded from the seeding side (bottom of the image) into approximately a half thickness of the scaffold with 300- μm pores. Fig. 7h shows the quantification of average cell penetration depths in the two types of scaffolds, where different rates and degrees of cell invasion could be efficiently observed. Therefore, PAM can function as virtual biopsy to non-invasively monitor the interaction between cells and scaffolds, unlike conventional histology methods, which require physical sectioning of the construct in a destructive manner.

Photoacoustic microscopy of neovascularization in scaffolds *in vivo*

Angiogenesis is a crucial step in the process of natural wound healing or tissue repairing [6]. It is also important in regenerative medicine especially for the engineering of thick or highly vascularized tissues such as liver and myocardium, to provide sufficient supplies of nutrients and oxygen to cells residing in the bulk of a scaffold [7,83]. Recently, PAM has been demonstrated for non-invasive imaging and monitoring of the neovascularization process in individual porous scaffolds *in vivo* up to 6 weeks post implantation [84].

PLGA inverse opal scaffolds (pore size: $\sim 200 \mu\text{m}$; dimensions: $\sim 3 \text{ mm} \times 3 \text{ mm} \times 1.5 \text{ mm}$) were implanted subcutaneously in the ears of nude mice, and then monitored using a dual-modality OR-PAM/OCT system [85] for 6 weeks. The dual-modality system was able to simultaneously image and analyze the vasculature and the scaffolds. As shown by the coronal MAP PAM images in Fig. 8a–c, the density of blood vessels increased with time over the 6-week period. Microvasculature down to the capillary level could be

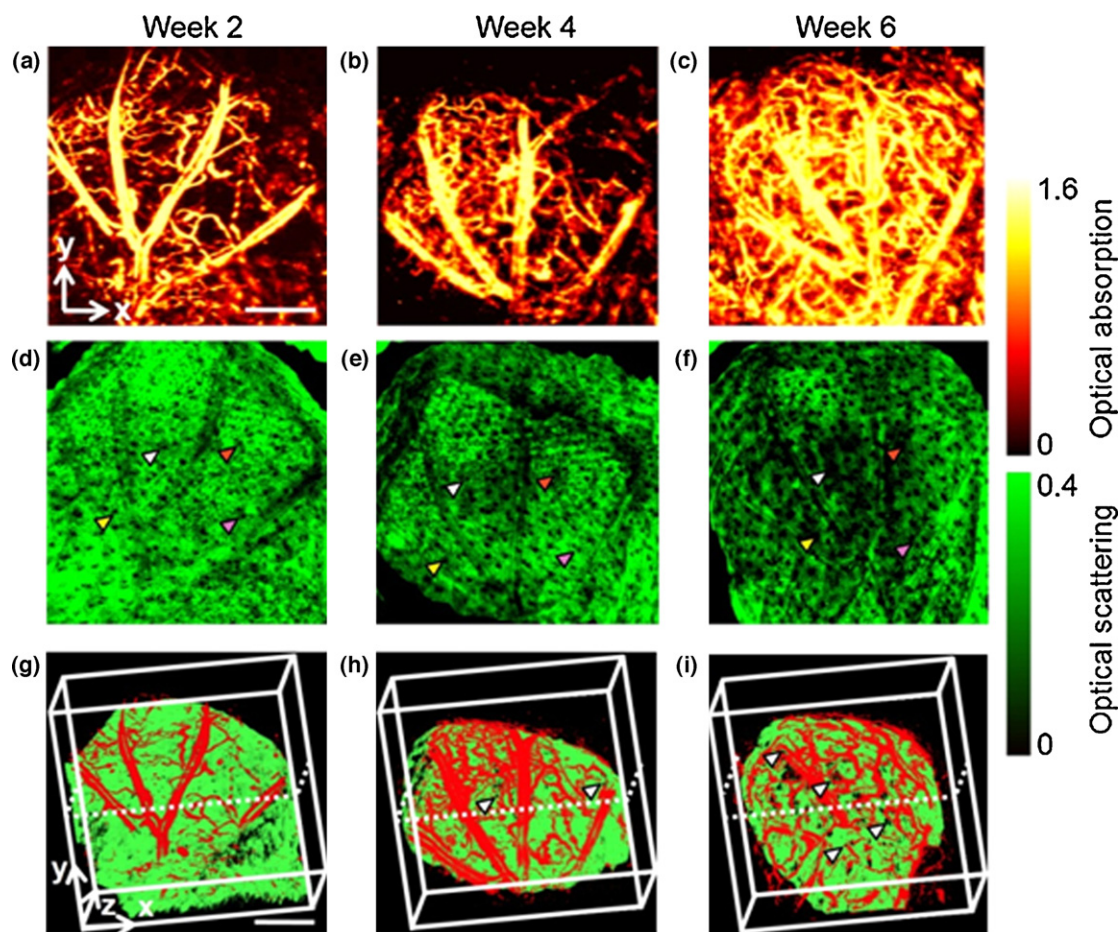
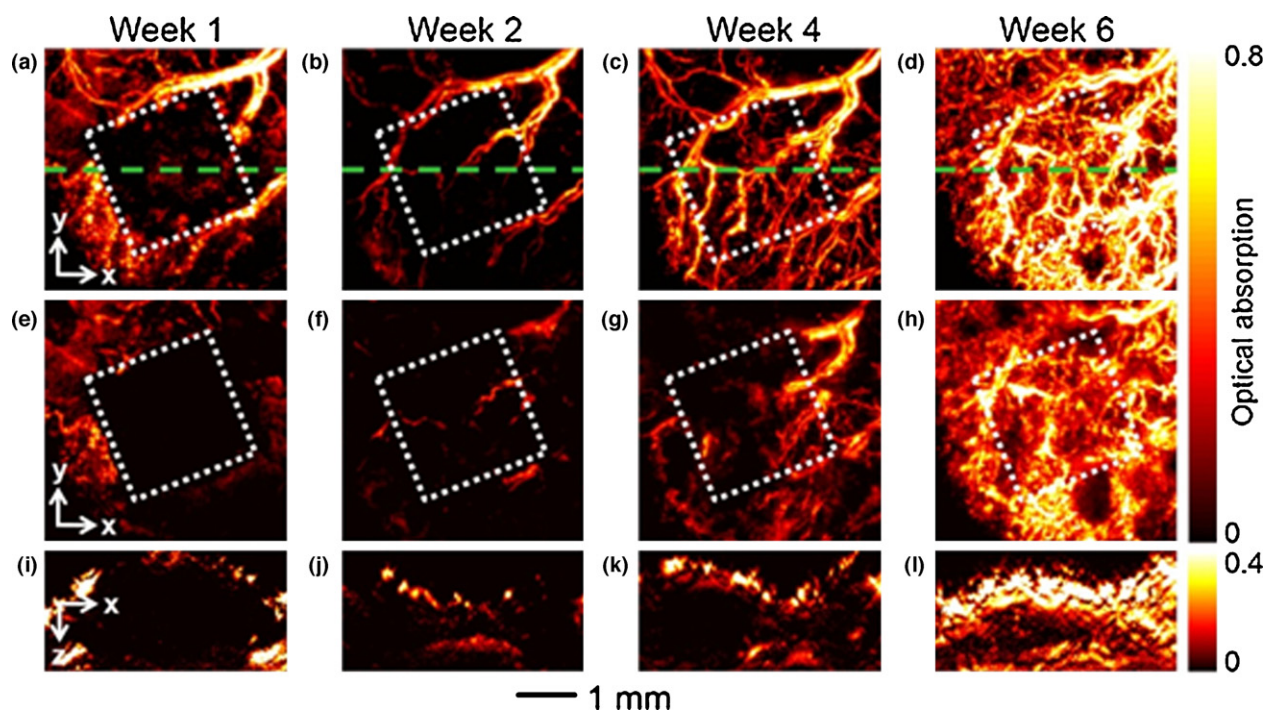


FIGURE 8

Chronological OR-PAM and OCT images showing the vasculature and scaffold/tissue construct for an inverse opal scaffold with a pore size of 200 μm implanted in a mouse ear model. (a–c) MAP PAM images showing the development of blood vessels at 2, 4 and 6 weeks post-implantation, respectively. (d–f) The corresponding OCT MAP images showing the scaffold/tissue construct. The signals from the skin layer were removed from all the OCT images to show the surface of the scaffold more clearly. Arrowheads indicate examples of local increase in pore size over time because of degradation of the scaffold. (g–i) Co-registered 3D depictions of the vasculature (red) and scaffold/tissue construct (green) at 2, 4 and 6 weeks post-implantation, respectively. The arrowheads indicate the growth of neovascularization into the pores of the scaffold. Scale bars: 500 μm .

Reprinted with permission from Ref. [84]. Copyright 2011 Mary Ann Liebert, Inc.

**FIGURE 9**

Chronological AR-PAM images revealing the development of neovasculation in an inverse opal scaffold with a pore size of $200\ \mu\text{m}$ implanted in a mouse ear model. (a–d) MAP images without removing the signals from the skin layer on top of the scaffold at 1, 2, 4 and 6 weeks post-implantation, respectively. (e–h) Corresponding MAP images after removal of the signals from the skin layer on top of the scaffold. (i–l) The corresponding B-scan images at planes marked by the green dashed lines in (a–d), respectively. The dotted square indicates the area where the scaffold resided. Reprinted with permission from Ref. [84]. Copyright 2011 Mary Ann Liebert, Inc.

well-resolved because of the high lateral resolution of OR-PAM. As shown by the MAP OCT images in Fig. 8d–f, collected simultaneously with PAM images, the position of the scaffold could also be well resolved. The signals from the skin layer were removed from all the OCT images to show the surface of the scaffold more clearly. Some regions of the scaffold had slightly degraded over the 6-week period, leading to a local increase in pore size (indicated by arrowheads). Fig. 8g–i shows co-registered 3D depictions of the vasculature (in red) and the scaffold/tissue construct (in green). The arrowheads indicate the growth of the neovasculation into the pores of the scaffold.

Deeper penetration could be further achieved using AR-PAM. At week 1, the scaffold region (indicated by the white dotted square) could be clearly observed because of the absence of blood vessels (Fig. 9a). The scaffold region could be better resolved in Fig. 9e after removal of the signals from the skin ($\sim 150\ \mu\text{m}$ in thickness) using a skin-removal algorithm [86]. As shown by Fig. 9b–d, the neovasculation developed gradually over time, consistent with the results from OR-PAM. These blood vessels not only grew on top of the implanted scaffold but also penetrated into the bulk of the scaffold (Fig. 9f–h, with removal of the signals from the skin). In addition, B-scan images (Fig. 9, i–l) at the indicated positions (green dotted lines in Fig. 9a–d) show increases both in photoacoustic amplitude and number of blood vessels in the central regions, confirming the inward growth of the neovasculation into the inner pores of the scaffold.

Quantifications of normalized vessel area as functions of time are shown in Fig. 10a and b. The area of blood vessels at each time point was normalized against that of the scaffolds with a pore size of

$80\ \mu\text{m}$ at week 2. The PAM results show that the normalized vessel areas for the scaffolds with a pore size of $200\ \mu\text{m}$ was 2.0–3.5 times larger than those of the scaffolds with a pore size of $80\ \mu\text{m}$ over a period of 6 weeks, which correlated well with the conventional, invasive histology analyses where complicated sectioning processes are involved. The development of neovasculation close to the surface (0 – $200\ \mu\text{m}$) of the scaffold was also examined using the PAM data. In both types of scaffolds, there were vessels with large areas, and the vessel areas were estimated to be ~ 1.9 times and ~ 3.7 times larger than those in the central region of the scaffolds with pore sizes of $200\ \mu\text{m}$ and $80\ \mu\text{m}$, respectively (Fig. 10c). Similar results were obtained by analyzing the histology data.

Future developments

PAT/PAM is expected to find broad applications in imaging 3D scaffold-based samples for regenerative medicine. PAT can even image objects in biological tissues as deep as $\sim 7\ \text{cm}$ at the expense of decreasing lateral resolution [23], which may be sufficient to fit the ultimate goal of engineering tissues with large volumes. Functional PAM can also be performed to derive other important parameters (*e.g.* flow velocity, oxygen saturation, oxygen partial pressure, and metabolite of oxygen) of the neovasculation [87–90].

PAT/PAM still has multiple technical challenges. For high-speed multi-contrast PAM based on spectroscopy, high-sensitivity acoustic arrays and high-repetition lasers with fast wavelength-tuning at each scan position must be developed. Multiscale PAT bridges the gap of a complex biological system between the microscopic and macroscopic domains through consistent optical absorption

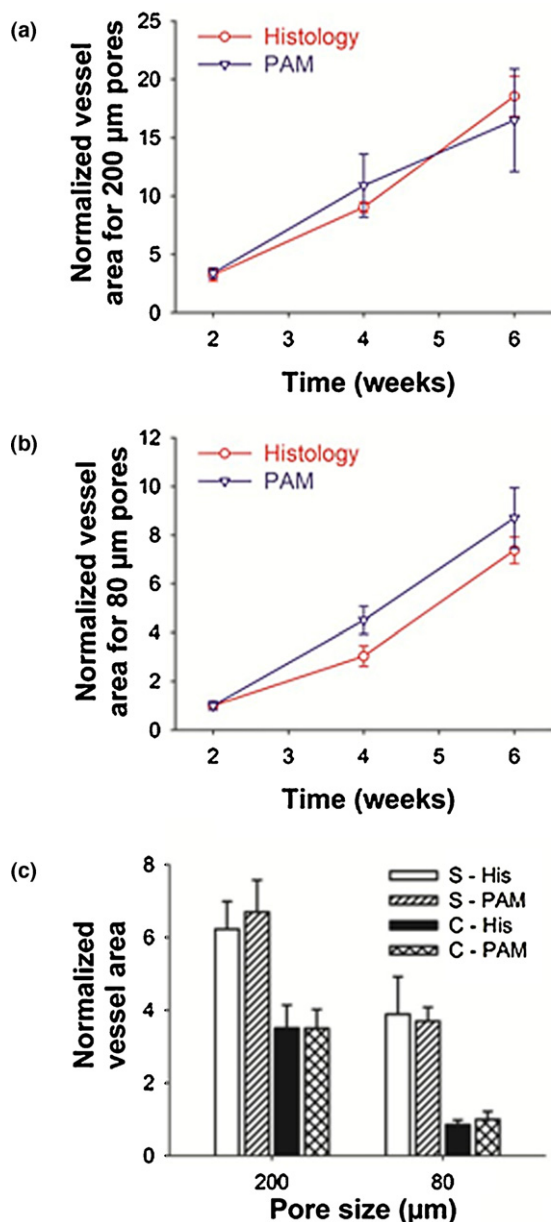


FIGURE 10

Comparison of histology analyses and PAM quantification. **(a and b)** Normalized vessel area calculated from both PAM data and histology for scaffolds with a pore size of (a) 200 μm and (b) 80 μm. **(c)** A comparison of the blood vessel area in the scaffolds at planes close to the surface and in the central region of the scaffolds 6 weeks post-implantation. S: surface; C: center; His: histology. All the results were presented as mean ± standard error ($n = 3$).

Reprinted with permission from Ref. [84]. Copyright 2011 Mary Ann Liebert, Inc.

contrasts. Thus, an integrated single PAT system with a large range of switchable resolutions and penetration depths is of great interest [91]. It is expected that further advancement of this fast-growing imaging modality will find even broader applications for tissue engineering and regenerative medicine, especially when thick scaffold/tissue constructs are involved.

Acknowledgements

We are grateful to Sandra Matteucci for close reading of the manuscript. Our work was supported in part by an NIH Director's

Pioneer Award (DP1 OD000798) and startup funds from Georgia Institute of Technology (to Y.X.). Our work was also sponsored by NIH grants R01 EB000712, R01 EB008085, R01 CA140220, R01 CA157277, R01 CA159959, U54 CA136398, and DP1 EB016986 – NIH Director's Pioneer Award (to L.V.W.). L.V.W. has a financial interest in Microphotoacoustics, Inc. and Endra, Inc., which, however, did not support this work. Others claim no competing financial interests.

References

- [1] R. Langer, J.P. Vacanti, *Science* 260 (5110) (1993) 920.
- [2] R. Langer, et al. *Tissue Eng.* 1 (2) (1995) 151.
- [3] R. Langer, *Adv. Mater.* 21 (32–33) (2009) 3235.
- [4] P.X. Ma, *Mater. Today* 7 (5) (2004) 30.
- [5] S.J. Hollister, *Nat. Mater.* 4 (7) (2005) 518.
- [6] Z.S. Patel, A.G. Mikos, *J. Biomater. Sci. Polym. Ed.* 15 (6) (2004) 701.
- [7] M. Lovett, et al. *Tissue Eng. B: Rev.* 15 (3) (2009) 353.
- [8] V. Karageorgiou, D. Kaplan, *Biomaterials* 26 (27) (2005) 5474.
- [9] S.W. Choi, et al. *Langmuir* 26 (24) (2010) 19001.
- [10] S. Yang, et al. *Tissue Eng.* 7 (6) (2001) 679.
- [11] S. Yang, et al. *Tissue Eng.* 8 (1) (2002) 1.
- [12] X. Cai, et al. *Tissue Eng. C: Methods* 18 (4) (2012) 310.
- [13] S.M. Dorsey, et al. *Biomaterials* 30 (16) (2009) 2967.
- [14] G.H. van Lenthe, et al. *Biomaterials* 28 (15) (2007) 2479.
- [15] C. Schmidt, et al. *Biomaterials* 30 (30) (2009) 5959.
- [16] J. Goldstein, et al., *Scanning Electron Microscopy and X-ray Microanalysis*, 3rd ed., Springer, Berlin, 2003p. 689.
- [17] D.M. Shotton, *J. Cell Sci.* 95 (3) (1990) 1.
- [18] C.K. Perng, et al. *J. Surg. Res.* 168 (1) (2011) 9.
- [19] D. Dumas, et al. in: A. Continuum, J. Buckwalter, et al. (Eds.), *Osteoarthritis, Inflammation and Degradation*, IOS Press, Amsterdam, 2007, p. 254.
- [20] Y. Yang, et al. *Phys. Med. Biol.* 51 (7) (2006) 1649.
- [21] K. Potter, et al. *Bone* 38 (3) (2006) 350.
- [22] I.A. Peptan, et al. *Tissue Eng.* 12 (4) (2006) 843.
- [23] L.V. Wang, S. Hu, *Science* 335 (6075) (2012) 1458.
- [24] C. Kim, et al. *Chem. Rev.* 110 (5) (2010) 2756.
- [25] P. Beard, *Interface Focus* 1 (4) (2011) 602.
- [26] S.Y. Emelianov, et al. *Phys. Today* 62 (8) (2009) 34.
- [27] K. Wilson, et al. *Nat. Commun.* 3 (2012) 618.
- [28] L.V. Wang, *Nat. Photon.* 3 (9) (2009) 503.
- [29] S. Oladipupo, et al. *Proc. Natl. Acad. Sci. U. S. A.* 108 (32) (2011) 13264.
- [30] C. Kim, et al. *ACS Nano* 4 (8) (2010) 4559.
- [31] S. Hu, et al. *Opt. Lett.* 35 (1) (2010) 1.
- [32] X. Cai, et al. *PLoS ONE* 7 (8) (2012) e43999.
- [33] X. Wang, et al. *J. Neurosci. Methods* 168 (2) (2008) 412.
- [34] T.N. Erpelding, et al. *Radiology* 256 (1) (2010) 102.
- [35] C.P. Favazza, et al. *J. Biomed. Opt.* 16 (1) (2011) 016015.
- [36] L. Nie, et al. *J. Biomed. Opt.* 17 (11) (2012) 110506.
- [37] H.F. Zhang, et al. *Nat. Biotechnol.* 24 (7) (2006) 848.
- [38] X. Wang, et al. *Nat. Biotechnol.* 21 (7) (2003) 803.
- [39] J.M. Yang, et al. *Nat. Med.* 18 (2012) 1297.
- [40] Laser Institute of America, American National Standard for the Safe Use of Lasers ANSI Z136.1-2007, American National Standards Institute Inc., New York, 2007.
- [41] S. Hu, L.V. Wang, *Front. Neuroenergy* 2 (2010) 10.
- [42] C. Zhang, et al. *J. Biomed. Opt.* 17 (11) (2012) 116016.
- [43] L. Wang, et al. *J. Biomed. Opt.* 17 (10) (2012) 106007.
- [44] S. Hu, et al. *Opt. Lett.* 36 (7) (2011) 1134.
- [45] K. Maslov, et al. *Opt. Lett.* 33 (9) (2008) 929.
- [46] C. Zhang, et al. *Opt. Lett.* 35 (19) (2010) 3195.
- [47] D.K. Yao, et al. *Opt. Lett.* 35 (24) (2010) 4139.
- [48] C. Zhang, et al. *J. Biomed. Opt.* 18 (2) (2013) 020504.
- [49] K. Maslov, et al. *Opt. Lett.* 30 (6) (2005) 625.
- [50] F.A. Duck, *Physical Properties of Tissue: A Comprehensive Reference Book*, Academic Press, London, 1990p. 346.
- [51] N. Artzi, et al. *Nat. Mater.* 10 (9) (2011) 704.
- [52] A.A. Appel, et al. *Tissue Eng. C: Methods* 18 (11) (2012) 859.
- [53] H. Nitzsche, et al. *Tissue Eng. C: Methods* 15 (3) (2009) 513.
- [54] L. Solorio, et al. *Theranostics* 2 (11) (2012) 1064.
- [55] X. Shi, et al. *Biomaterials* 28 (28) (2007) 4078.
- [56] M. Pramanik, et al. *J. Biomed. Opt.* 14 (3) (2009) 034018.

- [57] P.W. Barone, et al. *Nat. Mater.* 4 (1) (2005) 86.
- [58] M.J. O'Connell, et al. *Science* 297 (5581) (2002) 593.
- [59] S. Pahl, <http://omlc.ogi.edu/spectra/hemoglobin/index.html>, 1999
- [60] R.M. Weight, et al. *Opt. Lett.* 31 (20) (2006) 2998.
- [61] Y. Wang, et al. *J. Biomed. Opt.* 16 (1) (2011) 011014.
- [62] J.T. Oh, et al. *J. Biomed. Opt.* 11 (3) (2006) 34032.
- [63] S.W. Choi, et al. *Adv. Mater.* 21 (29) (2009) 2997.
- [64] S.W. Choi, et al. *Small* 5 (4) (2009) 454.
- [65] Y. Zhang, et al. *Biomaterials* 31 (33) (2010) 8651.
- [66] S.W. Choi, et al. *Langmuir* 26 (14) (2010) 12126.
- [67] Y. Zhang, Y. Xia, *Adv. Funct. Mater.* 22 (1) (2012) 121.
- [68] Y. Zhang, et al. *Macromol. Rapid Commun.* 33 (4) (2012) 296.
- [69] C.R. Parish, *Immunol. Cell Biol.* 77 (6) (1999) 499.
- [70] R. Yuste, *Nat. Methods* 2 (12) (2005) 902.
- [71] D. Razansky, et al. *Nat. Photon.* 3 (7) (2009) 412.
- [72] G.S. Filonov, et al. *Angew. Chem. Int. Ed. Engl.* 51 (6) (2012) 1448.
- [73] L. Li, et al. *J. Biomed. Opt.* 12 (2) (2007) 020504.
- [74] A. Krumholz, et al. *J. Biomed. Opt.* 16 (8) (2011) 080503.
- [75] D. Pan, et al. *Contrast Media Mol. Imaging* 6 (5) (2011) 378.
- [76] E.C. Cho, et al. *Angew. Chem. Int. Ed. Engl.* 52 (4) (2013) 1152.
- [77] Y. Zhang, et al. *Theranostics* (2012).
- [78] S.Y. Nam, et al. *PLoS ONE* 7 (5) (2012) e37267.
- [79] Y. Zhang, et al. *Theranostics* (2013), <http://dx.doi.org/10.7150/thno.5369>.
- [80] Y. Zhang, et al. *Angew. Chem. Int. Ed. Engl.* 50 (32) (2011) 7359.
- [81] T. Mosmann, *J. Immunol. Methods* 65 (1–2) (1983) 55.
- [82] M. Berridge, A.S. Tan, *Arch. Biochem. Biophys.* 303 (2) (1993) 474.
- [83] R.K. Jain, et al. *Nat. Biotechnol.* 23 (7) (2005) 821.
- [84] X. Cai, et al. *Tissue Eng. C: Methods* 19 (3) (2012) 196.
- [85] L. Li, et al. *Opt. Express* 17 (19) (2009) 16450.
- [86] H.F. Zhang, et al. *J. Biomed. Opt.* 14 (2) (2009) 024050.
- [87] J. Yao, et al. *Opt. Lett.* 35 (9) (2010) 1419.
- [88] J. Yao, L.V. Wang, *J. Biomed. Opt.* 15 (2) (2010) 021304.
- [89] Y. Wang, et al. *Opt. Lett.* 36 (7) (2011) 1029.
- [90] J. Yao, et al. *J. Biomed. Opt.* 16 (7) (2011) 076003.
- [91] W. Xing, et al. *Opt. Lett.* 38 (1) (2013) 52.